Volumetric Bioprinting of Organoids and Optically Tuned Hydrogels to Build Liver-Like Metabolic Biofactories

Paulina Nuñez Bernal, Manon Bouwmeester, Jorge Madrid-Wolff, Marc Falandt, Sammy Florczak, Nuria Ginés Rodriguez, Yang Li, Gabriel Größbacher, Roos-Anne Samsom, Monique van Wolferen, Luc J. W. van der Laan, Paul Delrot, Damien Loterie, Jos Malda, Christophe Moser, Bart Spee, and Riccardo Levato*

Organ- and tissue-level biological functions are intimately linked to micro-scale cell–cell interactions and to the overarching tissue architecture. Together, biofabrication and organoid technologies offer the unique potential to engineer multi-scale living constructs, with cellular microenvironments formed by stem cell self-assembled structures embedded in customizable bioprinted geometries. This study introduces the volumetric bioprinting of complex organoid-laden constructs, which capture key functions of the human liver. Volumetric bioprinting via optical tomography shapes organoid-laden gelatin hydrogels into complex centimeter-scale 3D structures in under 20 s. Optically tuned bioresins enable refractive index matching of specific intracellular structures, countering the disruptive impact of cell-mediated light scattering on printing resolution. This layerless, nozzle-free technique poses no harmful mechanical stresses on organoids, resulting in superior viability and morphology preservation post-printing. Bioprinted organoids undergo hepatocytic differentiation showing albumin synthesis, liver-specific enzyme activity, and remarkably acquired native-like polarization. Organoids embedded within low stiffness gelatins (<2 kPa) are bioprinted into mathematically defined lattices with varying degrees of pore network tortuosity, and cultured under perfusion. These structures act as metabolic biofactories in which liver-specific ammonia detoxification can be enhanced by the architectural profile of the constructs. This technology opens up new possibilities for regenerative medicine and personalized drug testing.

1. Introduction

Laboratory-made 3D living constructs that fully retain the function of human tissues and organs remain a major hope for regenerative medicine and for the development of advanced in vitro models for drug discovery, toxicology testing, and precision medicine.[1,2] Biofabrication approaches, thanks to their ability to precisely orchestrate the 3D patterning of multiple types of cells and biomaterials, have great potential to generate key architectural elements that can instruct the emergence of native functionalities in engineered tissues.[2] To date, various bioprinting techniques, a subset of biofabrication approaches in which one or several cellular components are directly incorporated in an additive manufacturing process,[3] have played a primary role in several proof-of-concept applications that showed the mimicry of salient organ functions in vivo, including in engineered ovaries,[4] thyroid glands,[5] and innervated skeletal muscle-like constructs.[6] The versatility and the freedom of design guaranteed

P. N. Bernal, S. Florczak, N. G. Rodriguez, Y. Li, G. Größbacher, J. Malda, R. Levato
Department of Orthopaedics
University Medical Center Utrecht
Utrecht University
Utrecht 3584CX, The Netherlands
E-mail: r.levato@uu.nl

M. Bouwmeester, M. Falandt, R.-A. Samsom, M. van Wolferen, J. Malda, B. Spee, R. Levato
Department of Clinical Sciences
Faculty of Veterinary Medicine
Utrecht University
Utrecht 3584CT, The Netherlands

J. Madrid-Wolff, C. Moser
Laboratory of Applied Photonics Devices
École Polytechnique Fédéral Lausanne (EPFL)
Lausanne CH-1015, Switzerland

L. J. W. van der Laan
Department of Surgery
Erasmus MC-University Medical Center
Rotterdam 3015GD, The Netherlands

P. Delrot, D. Loterie
Readily3D SA
EPFL Innovation Park, Building A, Lausanne CH-1015, Switzerland

by bioprinting technologies can be exploited both to generate anatomical-like as well as engineering-inspired architectures. While the exact degree of biomimicry that an engineered tissue should have right after the fabrication step is still a matter of debate, it is generally agreed that recapitulating every detail of physiological structures may not be needed, while providing cells with an environment to initiate and boost their own biological functionality is more important.[4,5,7,8] However, developing complex living structures of physiologically relevant size (i.e., dimension above the centimeter-scale) that can favorably guide cell behavior remains a major challenge. In addition, while bioprinting excels at modulating the environment surrounding the printed cells, tissue morphogenesis events in vivo are primarily driven by cell–cell interactions and self-assembly at the microscale, and thus cannot be directly controlled in a bioprinting strategy. Thanks to the development of organoids, which are miniaturized 3D structures that express key organ-like behavior, harnessing such cell-driven organization in vitro has led to a major breakthrough in biomedical research.[9] Even though organoids can also be generated from differentiated primary cells, most of the systems developed up to now arise from stem cells (harvested from adult tissue, or induced pluripotent cells).[10] Stem-cell derived systems are particularly promising due to their self-renewal capacity, helping to obtain sufficient organoid numbers for downstream applications, and due to the potential of the cells to differentiate into the multiple lineages that compose the tissue of reference.[10] However, organoid development in conventional tissue culture on Matrigel-like substrates is highly aleatory, offering no control over individual architecture, and resulting in sizes limited to the millimeter range.

In this work, we introduce a new, generalizable strategy for the light-driven volumetric bioprinting (VBP) of complex, functional organoid-laden constructs (**Figure 1**A). VBP is a layerless printing approach capable of printing positive and negative features (channels) at high resolutions (41.5 ± 2.9 µm and 104.0 ± 5.5 µm, respectively) (Figure 1B,C) and large-scale constructs previously achieving volumes of up to 4.14 cm^3 in less than 30 s.[11] Given the novelty of the technology and of its working principle, which relies on the precise delivery of multiple tomographic light projections onto a cell-laden photopolymer, little is still known on the interplay between the cells and the precisely patterned projected light as well as on the printability requirements that a biomaterial needs to fulfill. Thus, first we investigated a new technique to engineer the optical properties of cell-laden hydrogels for VBP and unraveled its impact on printing shape fidelity. Leveraging this knowledge, in the present study VBP is combined for the first time with organoids that exhibit a microscale multicellular structure. These are herein bioprinted into centimeter-scale structures with designed architectures that facilitate access to metabolites. To meet the large cell numbers required for the volumetric bioprinting process (in the range of tens of millions of cells, at the densities shown throughout this study), a dynamic spinner flask culture system is used to establish organoid structures from human tissue samples (Figure 1D). As a proof-of-concept, we demonstrate the fabrication of centimeter-scale hydrogel-based objects embedding human liver epithelial organoids, obtained from primary (stem) cells found in intrahepatic bile ducts.[8] Differently from

dense aggregates obtained from differentiated hepatic cells, that do not usually acquire native microarchitectural features of the liver,[14] these organoids are epithelial in nature, and form a cyst-like structure with an inner hollow lumen surrounded by a thin cell (mono)layer (Figure 1D).[13] This specific organization is especially interesting since many liver functions are dependent on hepatocyte polarization, that is, the directional transfer and secretion of compounds from and toward the apical or basolateral side of the cell. Importantly, since the specialized microarchitecture of the organoids can be easily compromised by mechanical stresses, a particular attention was placed on the ability of the printing process to preserve the self-organization of these biological building units. Thus, in this work, epithelial liver organoids were selected to study how they can act as metabolically active biofactories, in which a prominent detoxification function of the liver can be modulated by the overall architecture of the construct, as defined via the volumetric printing process (Figure 1E).

2. Results and Discussion

Volumetric bioprinting is an emerging light-based technology capable of sculpting cell-laden photoresponsive hydrogels—also termed bioresins—into 3D constructs of various sizes, ranging up to several cubic centimeters, and complex geometries in a layerless fashion.[11] Leveraging the principles of tomographic additive manufacturing,[15,16] in VBP, a vat containing the bioresin is illuminated with visible light from multiple angles using a sequence of filtered back projections of the object to be printed. While the light patterns address the whole build volume, the cumulative energy dose provided by the projections exceeds the bioresin's photocrosslinking threshold only in the geometry corresponding to the programmed object, thus building the whole construct at once. In this way, VBP yields centimeter-scale structures embedding microscale features in tens of seconds.[17] The rapid fabrication time and cell-friendly light doses are beneficial for preserving cell viability and functionality post-printing, whereas extensive printing times required to fabricate large parts can be of concern for conventional layer-by-layer manufacturing (i.e., extrusion- and lithographic-based methods).[18] Moreover, via VBP, elements like overhangs, moving parts, and convoluted porous networks typical of native tissues, can be easily recapitulated without the need for sacrificial or support materials, as previously reported reproducing the trabecular meshwork of cancellous bone.[17]

As the first step toward the fabrication of organoid-laden structures, we investigated the impact of the optical properties of the bioresin on printing resolution, in particular the ability of the cell-laden material to homogenously transmit light. As opposed to extrusion-based bioprinting (EBB), in which printability is predominantly governed by the rheological properties of a bioink,[19–22] in VBP and other light-based approaches, such as stereolithography and digital light processing, the printing resolution is defined primarily by the photopolymerization kinetics of the material, and by the ability to precisely control the spatial distribution of the light dose within the bioresin volume. While EBB of photocrosslinkable materials requires rapid polymerization kinetics as well to ensure construct stability,
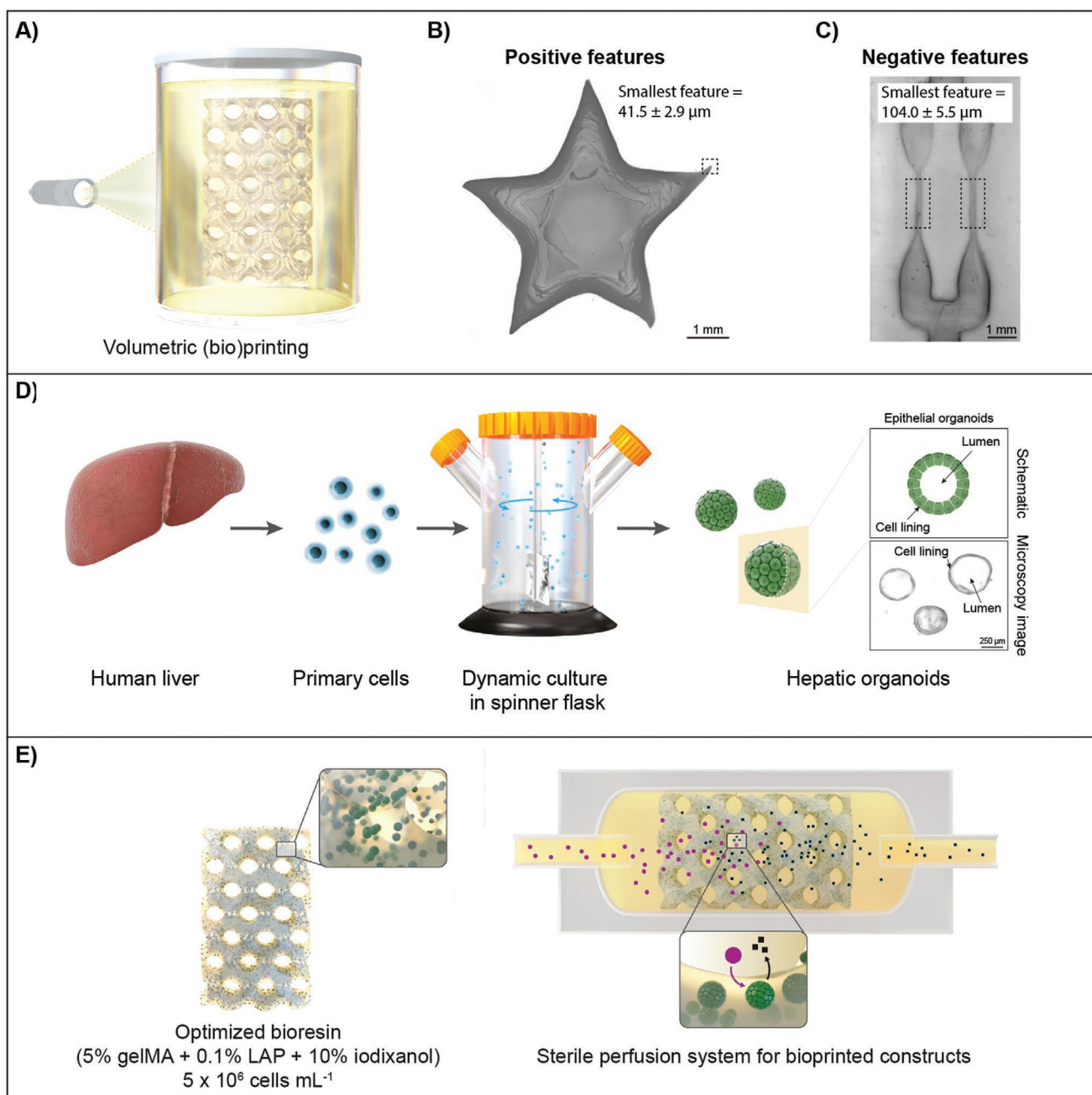
Figure 1. Overview of the high-resolution volumetric printing process and study design. A) Schematic representation of the volumetric printing process. B,C) Highest-resolution prints of positive (B) and fully perfusable negative (B) features achieved with the 5% gelMA + 0.1% LAP bioresin used in this study (scale bars = 1 mm). Samples are imaged when being immersed in PBS directly after printing. D) Diagram of the hepatic organoid culture system, starting with human liver biopsies and isolation into single cells, which are then dynamically cultured in a spinner flask system to establish high yields of hollow epithelial organoid structures (microscopy image scale bar = 250 μm). E) Illustration of a complex, organoid-laden printed biofactory cultured under dynamic perfusion to enhance hepatic function, showing a representation of the breakdown of perfused compounds (purple circles) into metabolites (black squares).

in VBP the latter is key in achieving highly accurate prints. This factor is largely dependent on the resolution of the light projection, the spatial coherence of the light source, the algorithm for generating the set of patterns (for a digital micromirror device (DMD), the optical resolution is given by the effective pixel size projected in the print volume), and the presence or absence of scattering elements. The latter is of particular relevance for bioprinting applications, since cells and many subcellular structures are capable of altering the path of incident light, either causing attenuation of ballistic photons or scattering, therefore affecting printing resolution. In particular, scattered light will blur the projected tomographic
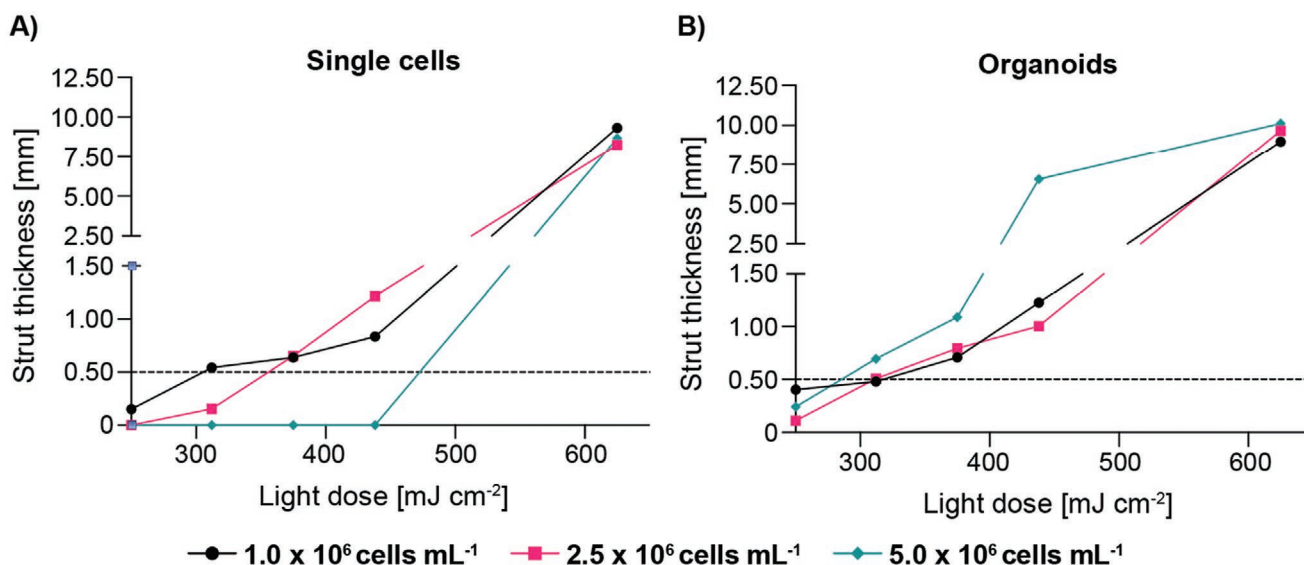
Figure 2. Effect of single-cell and organoid density on volumetric bioprinting accuracy in the absence of optical corrections. A,B) Fine feature thickness in constructs printed at increasing light doses (250–625 mJ cm^{-2}) with bioresins containing different densities of single cell (A) and organoid (B) (1–5 × 10^6 cells mL^{-1}). The dashed line represents the programmed feature dimension of the printed model (selected to be 500 μm to accommodate for the size of the printed organoids) ($n = 3$).

images, causing an increase of the light dose in regions of the volume adjacent, but external to the part to be printed. Depending on the length of the scattering mean free path at a given wavelength (which is a measurement of the average distance between two consecutive scattering events, thus inversely proportional to the cell density[23]), this can result in off-target polymerization and loss of resolution. In addition, the ballistic light attenuation caused by scattering decreases the addressable size of the construct in the vial.

To investigate this effect, we printed a 5% w/v gelatin methacryloyl (gelMA)-based bioresin (Figure S1, Supporting Information) supplemented with 0.1% w/v lithium phenyl-2,4,6-trimethylbenzoylphosphinate (LAP) as photoinitiator carrying either a single cell suspension of a well-known hepatic cell line (HepG2) (**Figure 2**A) or epithelial organoids derived from human liver (Figure 2B) in the form of a hollow disc with an S-shape filament (thickness = 500 μm) placed at its center (Figure S2, Supporting Information). This specific size was selected to generate filaments that could completely embed the produced organoids, even though finer printing resolution are possible as shown before in Figure 1B,C, in which resolution superior to what is shown with volumetric printing up to date has been demonstrated.[15,16,24,25] In an ideal print, both the thick border of the disc and the thinner filament, herein used as a benchmark to quantify the printing resolution, should solidify at the same time after receiving the same, optimal light dose. Exceeding this optimal dose will cause overcuring of the fine feature, thickening of the filament wall, and eventually clogging of the disc. At a low cell density (1 × 10^6 individual cells mL^{-1}) the bioresin is photocrosslinked at an exposure dose of 250 mJ cm^{-2}, and the fine features can be correctly resolved (at 312 mJ cm^{-2}) with both single HepG2 cells and organoids. At higher cell concentrations, the minimal light dose required for crosslinking single cell suspensions rises, and the slope

of the dose–thickness curve rapidly increases, narrowing the ideal printing window. Consequently, with the currently available hardware and software, printing at high cell densities is possible (as previously shown with up to 10^7 articular cartilage progenitor cells mL^{-1}).[17] However, this requires a fine empirical adjustment of the delivered dose, which is often impractical when cells are available in limited amounts. A similar trend was observed for organoid-laden bioresins, although the printing process yielded a larger printability window compared to what was observed with single cells, as loss of shape fidelity in reproducing the fine feature was observed only at 5 × 10^6 cells mL^{-1} (Figure S3, Supporting Information), a cell density selected for this investigation due to its already proven suitability for functional liver tissue engineering studies.[26–35] This result can be explained by the fact that liver organoids form cyst-like, hollow structures delimited by an epithelial cell monolayer.[13] Due to their relatively large size (≈300 μm), organoids have a longer scattering mean free path, compared to single cell suspensions at any given equivalent cell concentration. Recent research efforts are introducing novel algorithms for tomographic printing that can correct for scattering events at the filtered projection-level, and thus ensure high resolution printing even in opaque media.[36] Although this has been only shown with resins carrying homogenously sized particles so far,[36] future translation to materials laden with cells, which have more complex light-scattering profiles, will help expand the range of applications of VBP.

Cell-mediated scattering can also be addressed from the biomaterial-design perspective, by tuning the optical properties of the bioresin. In this study, we introduced a biocompatible and water-miscible refractive index matching compound, iodixanol, in order to modulate the optical performance of the gelMA-based bioresins (**Figure 3**A). Iodixanol was selected as it was proven not to harm cellular structures and tissue components,
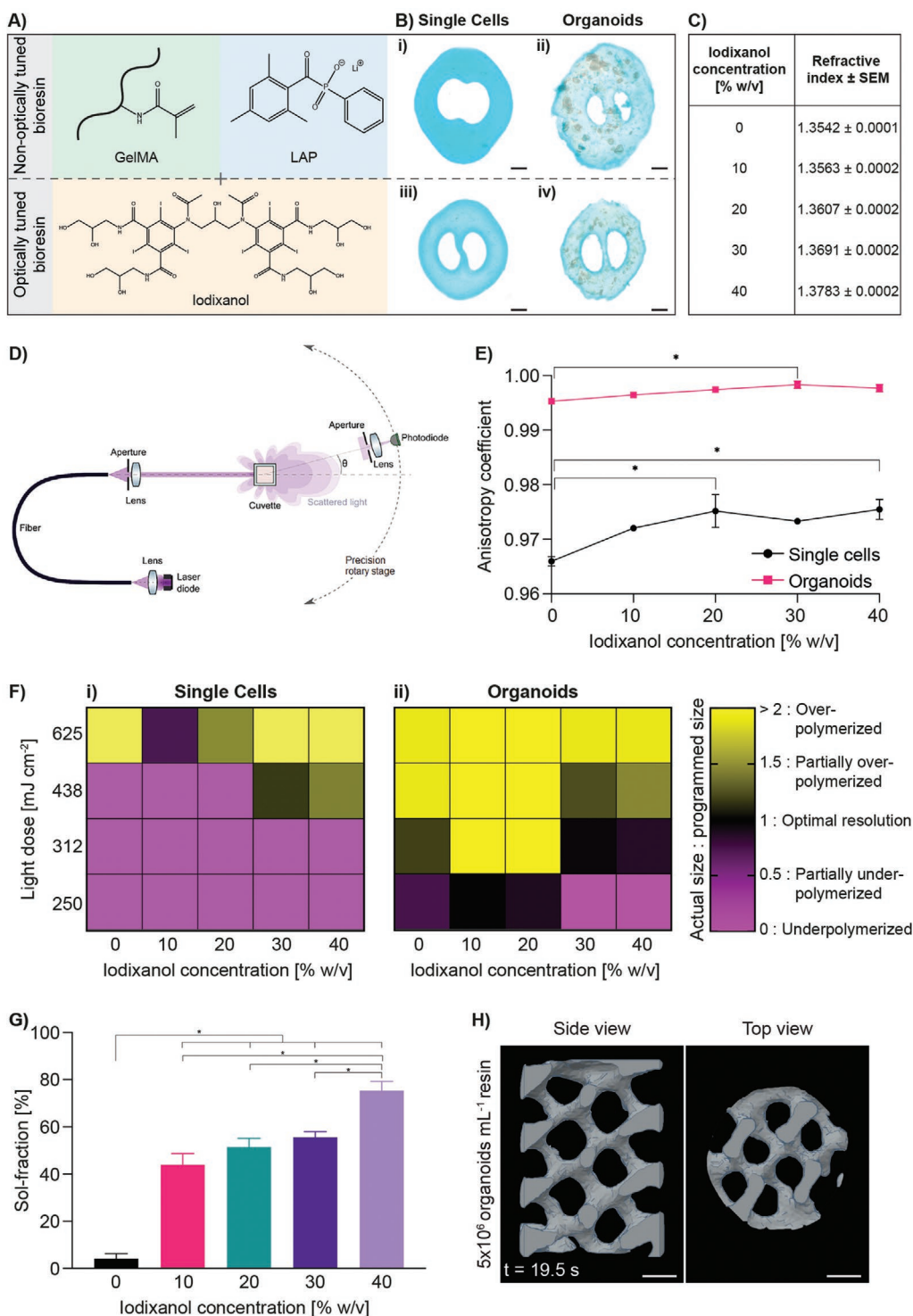
Figure 3. Enhancing volumetric bioprinting of single cells and hepatic organoids through bioresin optical tuning with iodixanol. A) Schematic of the bioresins used for volumetric bioprinting consisting of gelMA and LAP, supplemented with iodixanol to optically tune the bioresin for enhanced printing accuracy in the presence of cellular structures. B) Stereomicroscopy images of non-optically tuned bioresin (i,ii) and iodixanol-containing bioresins (iii,iv) for printing single cells and organoids (scale bars = 1 mm). C) Refractive index of the pristine and optically tuned bioresins ($n = 3$). D) Schematic of the light scattering measuring setup, and E) resulting anisotropy coefficient of different bioresin samples containing 5×10^6 mL^{-1} single cells and organoids and increasing iodixanol content ($n = 3$). F) Printability window of 5×10^6 mL^{-1} single cells and organoids represented by the ratio of the printed fine feature thickness to the programmed thickness ($n = 3$). G) Soluble fraction of gelMA samples containing increasing iodixanol concentrations ($n = 3$). H) Side and top view of cross-sections from the 3D reconstruction of a complex bioprinted gyroidal structure with the optimized bioresin formulation carrying 10% w/v iodixanol (scale bars = 2 mm). * = significant difference ($p < 0.05$).

**ADVANCED
SCIENCE NEWS**

www.advancedsciencenews.com

**ADVANCED
MATERIALS**

www.advmat.de

since this iodine, non-ionic compound has been applied for in vivo imaging,[37] as contrast agent for X-ray imaging,[38] and as an agent for the isolation of extracellular vesicles when preserving the integrity of membrane proteins is needed.[39] In principle, scattering-driven artefacts could be completely obviated, if the refractive index of the hydrogels matches that of the scattering element (i.e., the cells). However, cells are highly heterogeneous, composed of several subcellular structures each characterized by its own average refractive index (Table S1).[40] Furthermore, different cell types and even individual cells within the same population have a unique light scattering fingerprint. Selected concentrations of iodixanol could thus be tested to approximate the light refracting profile of key subcellular components that play a major role in light scattering at 405 nm (the wavelength used in the printer), which primarily includes the nucleus, contributing to increased ballistic light.[40]

Supplementation with iodixanol successfully improved printing resolution both when using bioresins embedding single cells or liver organoids at 5×10^6 cells mL^{-1} (Figure 3B), and it increased the refractive index of the bioresin in a concentration-dependent manner, from 1.352 (pristine gelMA) up to 1.3783 at a 40% w/v (Figure 3C). The characterization of the angular light scattering profile in bioresins laden with single cells and organoids, supplemented with increasing iodixanol concentrations (Figure 3D,E), confirmed the experimentally found result that more optical power was directed in the forward direction. The extracellular refractive index change caused by the addition of iodixanol provides a better match to the overall refractive index of the organoids and thus light is less scattered, which is indicated quantitatively by a measured anisotropy coefficient closer to 1 (unity indicates no scattering). This effect was observed for both single cells and organoids. In terms of volumetric bioprinting, this made it possible to identify a working window for printing hepatocytic cells of 30% w/v iodixanol and organoids with as low as 10% w/v iodixanol (Figure 3F, Figure S4, Supporting Information, statistical analyses in Tables S2 and S3, Supporting Information). Importantly, the positive effect of the printing optimization via hydrogel optical tuning can be readily applied to produce thin features also when utilizing higher cell densities (herein tested with 1.5×10^7 cells mL^{-1}). This was shown by printing star-shaped hydrogel structures with the smallest resolved points measuring 49.2 ± 8.4 and 50.5 ± 6.0 µm, when using single cells and organoids respectively, although the organoids, given their large size exceeding the minimum print resolution, may, of course, protrude from the gel in the proximity of the finest features (Figure S5, Supporting Information). Notably, this approach for optical tuning of the biomaterials could potentially be combined with upcoming software-end based algorithms to further enhance printing resolution.[36]

It should be noted that, while these results apply to the liver cells tested in this study, such optimization of the refractive index of the bioresin is likely to result in a different optimal printing window when utilizing another cell population. From the chemico-physical point of view, iodixanol is intended as a fugitive additive, and it passively diffuses out of the hydrogel after crosslinking. Sol-fraction analysis revealed that in presence of iodixanol concentrations from 10 to 40% w/v, the sol fraction of the bioresins increased from 44.0 ± 4.7% to 75.3 ± 3.9%, whereas pristine gelMA showed lower values (4.2 ± 2.1%) (Figure 3G). Such high values for the mass loss after 24 h can be explained by the partial diffusion of the refractive index matching compound out of the gels, but also indicate that part of the additive, which forms a viscous solution at room temperature, is likely still trapped in the gel and may be released over a longer time frame. Thus, to minimize the presence of this extra component in the culture environment and ensure hydrogel stability for the subsequent prints embedding liver organoids, the bioresin formulation containing the lowest amount of iodixanol (10% w/v) was selected. This optimized, optically tuned bioresin composition made it possible to resolve complex 3D structures, such as gyroidal constructs (Figure 3H) printed in under 20 s (195 mJ cm^{-2}, 19.5 s printing time), which are otherwise not possible to bioprint with conventional extrusion methods, especially with soft materials needed for tissue culture.

Having identified a bioresin formulation for printing with high shape fidelity in presence of increasing cell concentrations, we further explored the advantages of combining VBP and organoid technology to create a bioengineered construct able to perform native-like liver function, given the critical role of the liver in maintaining systemic homeostasis. Notably, the distinguishing ability of liver epithelial organoids to capture microscale level architectures present in the liver, together with the fact that they can be readily obtained from individual patients and healthy donors via minimally invasive biopsies, holds potential for the development of advanced in vitro models for drug discovery and toxicology in personalized medicine. Such new platforms are especially needed in biomedical research, as liver damage is a primary cause for post-marketing withdrawal of new drugs,[41] a situation accentuated by the fact that current animal and cell culture models are insufficient to fully predict human physiology or donor-dependent responses.[42,43] The performance of liver organoids within the selected hydrogel upon bioprinting via VBP was investigated. Given the inherent challenge in replicating the multifaceted biosynthetic functions of native hepatocytes in vitro, we specifically analyzed i) the viability of the printed structures, and ii) the influence of the VBP on organoid microstructure and morphology, as a preliminary step to promote the differentiation and maturation capacity of the printed construct into hepatic-like structures.

The liver organoids used in this study were originally derived from adult stem cells positive for EpCAM and for leucine-rich repeat-containing G-protein coupled receptor 5 (LGR5),[13] obtained through expansion in a dynamic stirred bioreactor.[44] Recent works further probing the in vivo origin of these cells suggest that these cells may be intrahepatic cholangiocytes, which display bi-potent differentiation capacity.[12] These adult cells have already been demonstrated to maintain genomic stability over multiple passages,[13] suggesting they can be an ideal source when high cell numbers are required for liver tissue engineering applications. As these hepatic organoids are available from donor tissues, they also have the potential for simulating a patient-specific response to drugs, as well as the production of catabolites or toxic compounds natively metabolized in the liver for drug discovery and toxicology studies, or serve as promising building blocks for whole organ engineering.[45]

**ADVANCED
SCIENCE NEWS**

www.advancedsciencenews.com

**ADVANCED
MATERIALS**

www.advmat.de

However, when freshly isolated and expanded, these cells do not normally display specific hepatocytic phenotype commitment.[12] The liver organoids obtained from these cells are typically expanded in presence of laminin-rich basal membrane extracts (i.e., Matrigel), in culture media cocktails that maintain them in a proliferative state. Their differentiation into hepatocytic structures is accompanied by an inhibition of proliferation and can be triggered by switching the media composition (key components being bone morphogenetic protein-7 and fibroblast growth factor-19).[44] This process has also been shown to be greatly influenced by mechano-chemical stimuli provided by different biomaterials and culture conditions.[46] As a first step, it was paramount to assess how organoids in differentiation media respond to the milieu defined by the VBP process.

Thus, upon printing, liver organoid-laden hydrogels were cultured in differentiation media. First, it was confirmed that iodixanol had no detrimental effect on the metabolic activity of the organoids, even when used in concentrations up to 40% w/v. In particular, all the tomographically bioprinted samples performed similarly to cast controls in absence of iodixanol, in which a slight decrement of resazurin reduction from day 1 to day 10 of culture was observed (**Figure 4**A). This was in line with what was previously observed for liver organoids cultured in differentiation conditions using other natural-origin hydrogels such as cellulose nanofibril-derived gels.[47]

The evolution of the metabolic activity over 10 days was also assessed in further detail with the optimized bioresin supplemented with 10% w/v iodixanol. The performance of constructs obtained from cells from three adult donors, was evaluated comparing samples generated via VBP, EBB, and cast gelMA (with and without iodixanol) and Matrigel controls to assess the impact of different fabrication approaches and materials (Figure 4B, further statistical details in Figure S6, Supporting Information). In all gelMA samples, the metabolic activity remained constant, whereas, in the Matrigel control, a gradual increase was observed over the culture period. In the latter, this increment was accompanied by a higher amount of DNA in the samples (Table S4, Supporting Information). This result is coherent with the notion that Matrigel is a favorable substrate for organoid proliferation.[47]

Having demonstrated the cytocompatibility of the bioresin and of the printing process, an important objective was to evaluate if VBP could be used to preserve organoid structure, including the specific cell–cell contacts, tight junctions, and communication channels established during the organoid formation phase. During the expansion phase, organoids can reach millimeter-scale sizes, and in general, the growth to larger dimensions is regarded as an indicator of cell health.[44] As a light-based biofabrication technology, VBP does not subject cells to potentially harmful shear stresses that can instead be experienced in nozzle-based techniques.[48] Moreover, in EBB, nozzles typically displaying diameters 2–3 times larger than these organoid structures are required in order to avoid clogging,[49] thus imposing a compromise on printing resolution. Alternatively, organoids need to be fragmented via mechanical or enzymatic disruption to enable seamless flow of the bioink during printing.

A live/dead fluorescent staining post-printing revealed that organoids printed via VBP displayed superior viability (93.3 ± 1.4%) and undisturbed average size (273.5 ± 49.9 µm) when compared to EBB (73.2 ± 1.2% viability, 100.1 ± 14.2 µm average size) one-day post-printing (Figure 4C–E). Such high viability, as demonstrated by the positive staining of Calcein AM into the cells lining the hollow organoid structures, was comparable or superior to cast gelMA and Matrigel controls. Notably, for all samples, it was found that most of the dead cells were single cells shed from the organoids, which appeared in higher numbers in the samples containing fragmented cells processed via EBB. This significant difference in dead cell numbers between the VBP conditions and the other processing methods can likely be attributed to the fact that the nozzle-free nature of VBP allows for the maintenance of the structural integrity of the organoids by minimizing the shear stresses induced on these large structures through actions such as pipetting or extruding through a nozzle. The EBB samples, which show the lowest viability at day 1, exhibit high number of dead cells likely due to i) a high number of single cells resulting from the mechanical fragmentation of the organoids pre-printing that are not capable of reassembly when incorporated in the hydrogels, and ii) further organoid damage and breakdown into single cells and smaller fragments due to the shear stresses experienced during extrusion through the nozzle (Figure 4D). This is further supported by the significantly smaller organoid sizes observed in EBB samples during the differentiation period (Figure 4E). Cast organoids in gelMA and Matrigel on the other hand, only undergo shear stresses as the embedded organoids pass through the narrow pipet tip for controlled volume deposition for the casting process, instead of the extensive fragmentation of EBB-printed organoids. This is likely the reason for the significantly higher viability compared to the EBB condition. Over time, viability values reached comparable values (94.1–98.2%) for all experimental groups and controls. This was predominantly due to the fact that dead cells are removed from the culture environment with each media exchange, paired with the preservation of the cell viability already discussed for the biomaterials used in this study. To date, organoid shaping via bioprinting has been demonstrated via extrusion of a suspension of single stem cells, which are then led to re-form into organoids post-printing.[50] Alternatively, biofabrication of pre-generated organoids has been prevalently performed via molding,[51] individual spheroid dispensing,[5] or robotic-assisted pick-and-place techniques.[52] Although yielding impressive results in terms of generating tissues with high cell content, these approaches are limited to relatively simple 3D geometries, and rely on the printing of thick filaments/spheroids with a 400–1000 µm diameter range to achieve simple tubular structures.[5,50–52] Complementing the possibilities granted by such strategies, the ability of VBP to print pristine, undamaged organoids offers an alternative to facilitate the free-form generation of intact organoid-laden constructs. Printing morphologically intact organoids can be advantageous for applications aiming to preserve the organoid pre-deposited ECM, given the increasing evidence that cells embedded in biomaterials alter their behavior via contact with the nascent, self-synthesized ECM.[53] Even though in the context of liver tissue engineering, hepatocytes alone have limited capacity to secrete extracellular matrix proteins, this could be relevant especially when incorporating other liver-specific cell types, such as stellate cells.[54]

Next, the expression of key hepatocyte differentiation markers was investigated (**Figure 5**). Organoids from all

**ADVANCED
SCIENCE NEWS**

www.advancedsciencenews.com

**ADVANCED
MATERIALS**

www.advmat.de
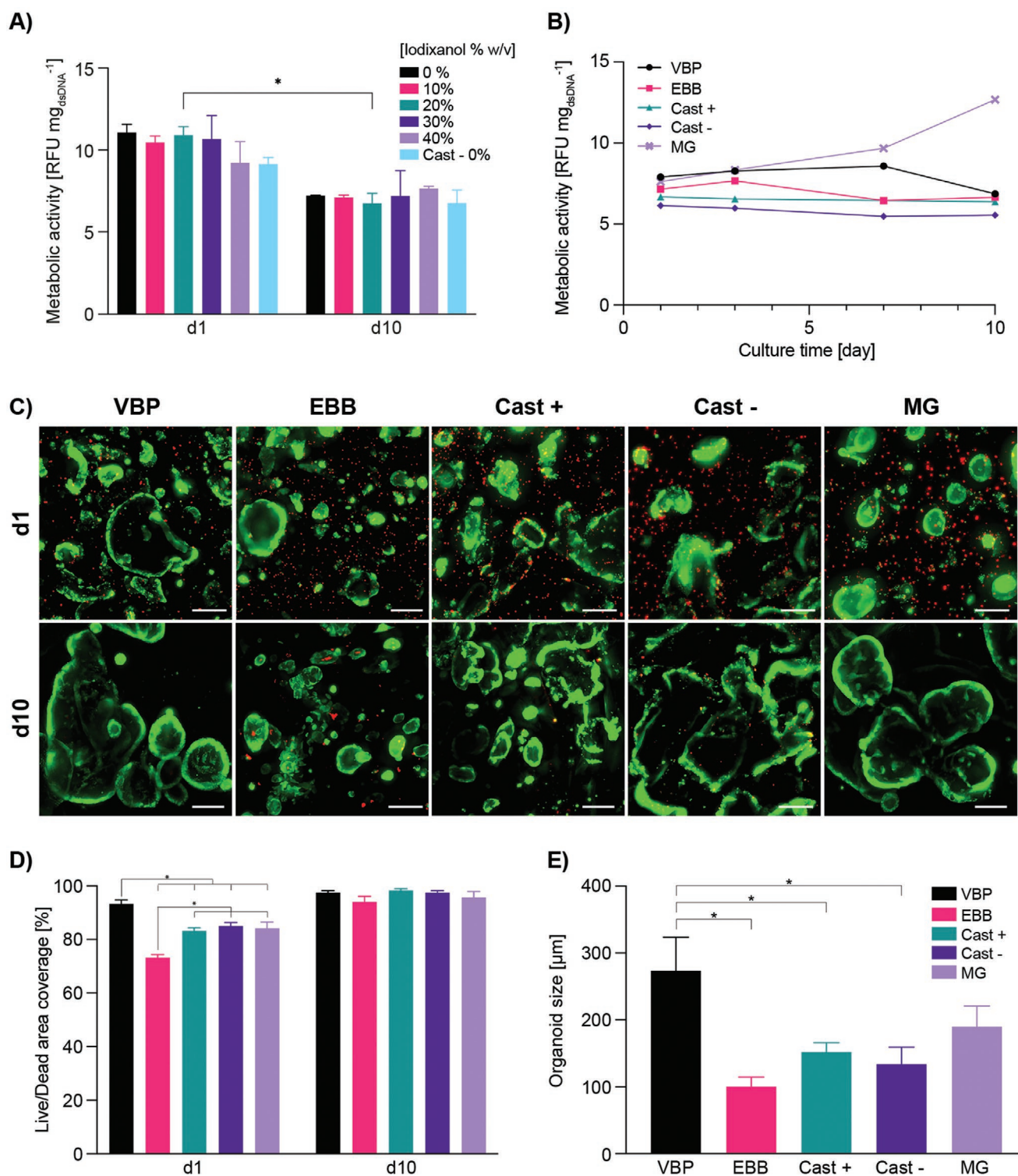
Figure 4. Viability of volumetrically bioprinted hepatic organoids. A) Metabolic activity of bioprinted organoids within bioresins with increasing iodixanol concentrations (0–40% w/v) over a 10-day differentiation period ($n = 5$). B) Metabolic activity ($n = 5$), C) representative live/dead images (scale bars = 250 µm), D) live-to-dead ratio area ($n = 3$) coverage, and E) average organoid sizes ($n = 60$) of VBP- and EBB-printed organoids with the optically tuned bioresin (gelMA + 10% w/v iodixanol), cast gelMA samples with (Cast +) and without 10% w/v iodixanol (Cast –) and cast Matrigel (MG) samples over a 10-day differentiation period. * = significant difference ($p < 0.05$).
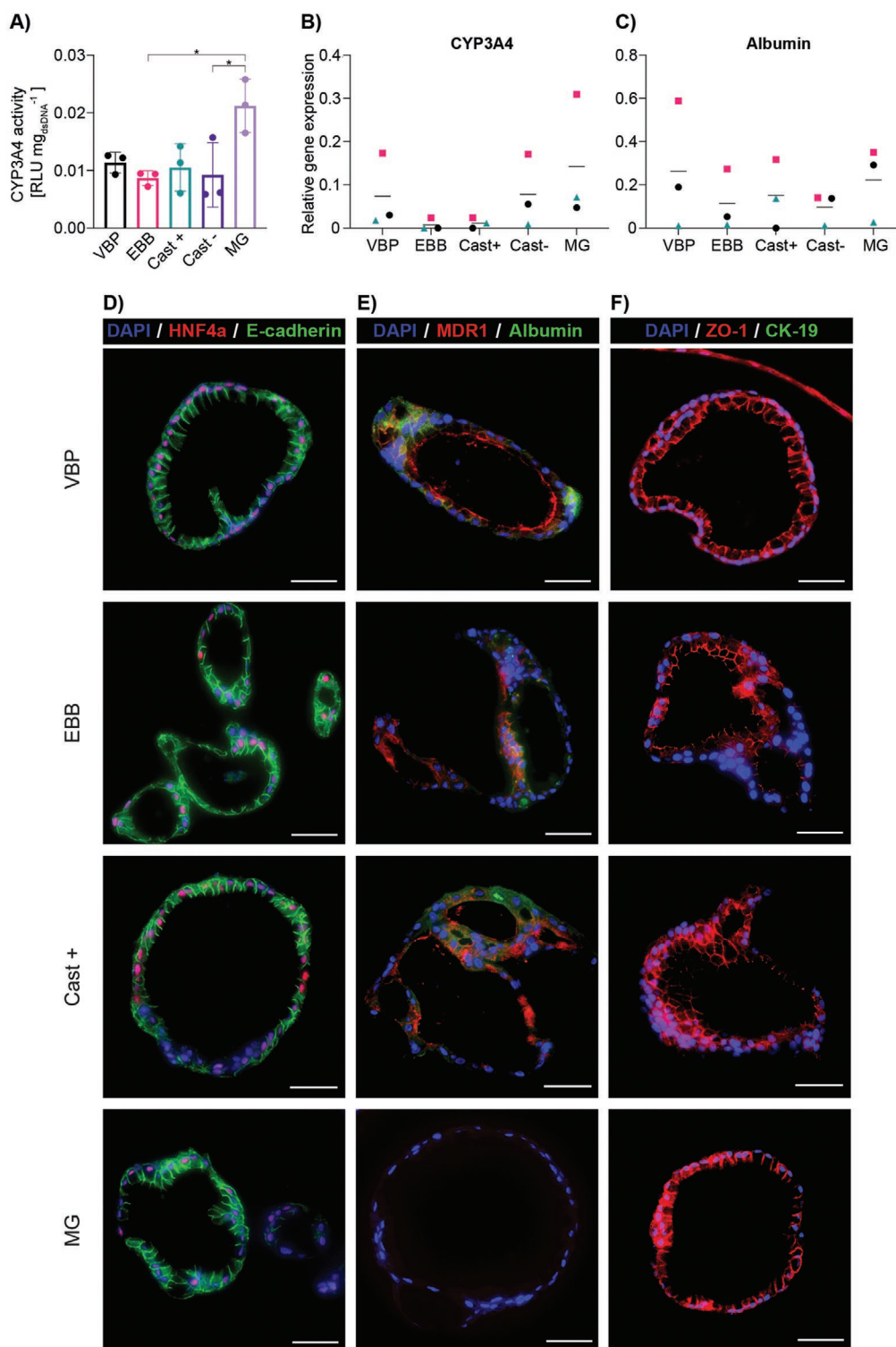
Figure 5. Liver-specific markers in volumetrically bioprinted hepatic organoids. A) CYP3A4 activity and B,C) relative gene expression of CYP3A4 (B) and albumin (C) in VBP- and EBB-printed organoids with the optically tuned bioresin, cast gelMA samples with (Cast +) and without 10% w/v iodixanol (Cast −) and cast Matrigel (MG) samples after a 10-day differentiation period (n = 3). D–F) Representative fluorescence images of liver-specific and organoid polarization markers HNF4α and E-cadherin (D), MDR1 and albumin (E), and CK19 and ZO-1 (F) in the VBP, EBB, Cast +, and MG conditions after 10 days of hepatic differentiation. Scale bars = 50 μm. Individual data points shown for 3 different donors (N = 3).* = significant difference (p < 0.05).

experimental groups showed comparable levels of cytochrome 3A4 activity (which appeared significantly elevated in Matrigel-based cultures versus EBB samples) normalized over the total protein content of the sample (Figure 5A), as well as gene expression levels of the same cytochrome and albumin (Figure 5B,C). In addition, all samples showed comparable normalized levels of various liver transaminases, such as aspartate transaminase (ASAT, involved in amino acid metabolism), gamma-glutamyl transferase (GGT, involved in drug and xenobiotic detoxification), and glutamate dehydrogenase (GLDH, involved in the urea cycle) (Figure S7, Supporting Information). The presence of such markers indicates the successful commitment toward a hepatocyte-like phenotype in VBP, EBB, and the cast controls, while only in the volumetrically bioprinted group this result was also paired with higher cell viability after printing. The evident donor-dependent variability observed in the expression levels indicates that liver organoids as in vitro models are better suited for personalized medicine applications or to establish bio-banks, for example, to study drug susceptibility on patient groups with similar genetic make-up, as already proposed for other tissue types.[55]

Immunofluorescence analysis of volumetrically bioprinted organoids within the optimized gelMA-based bioresin also revealed the intracellular presence of the hepatocyte markers hepatocyte nuclear factor 4 alpha (HNF4α), E-cadherin, high-expression of albumin and tight junction protein-1 (ZO-1) (Figure 5D–F), as well as the absence of the cholangiocyte marker cytokeratin 19 (CK-19),[44] underlining the acquisition of a hepatocyte-like phenotype. Organoid morphology and glycogen storage were also visualized in all experimental groups through hematoxylin and eosin (H&E) and periodic acid–Schiff (PAS) stainings (Figure S8, Supporting Information). Extrusion-based printed samples and castd controls also showed similar patterns, albeit with some key differences. In particular, the VBP samples clearly showed a significantly higher degree organoid polarization, with the formation of an apical side in the cyst lumen for the highest percentage of organoids (73.9 ± 1.8%), as evidenced by the localized expression of multidrug resistance protein 1 (MDR-1).[56] Organoid polarization is an indicator of maturation and an important feature to study the directional uptake, transport, and eventual secretion of metabolites present in the native liver, which is not observed in cell lines under conventionally established culture conditions (i.e., standard 2D culture of single liver cell lines, primary cells or 3D spheroid cultures). Moreover, while MDR-1 was also detected in EBB and cast gelMA controls (but not in Matrigel), quantitative analysis of the polarized organoids showed significantly impaired polarization in these groups (12.1 ± 1.2% for EBB, 36.9 ± 3.0% and 36.5 ± 3.6% 7 or the cast+ and cast- samples respectively) as opposed to VBP-printed organoids (Figure 5E, Figures S9 and S10, Supporting Information). This significant difference between VBP-printed organoids and EBB and cast controls could be attributed to the fact that in VBP, structural integrity of the organoids is not disrupted during the printing process and seemingly results in the rapid acquisition of polarity markers when the differentiation process begins. Instead, EBB and cast organoids undergo shear stresses and fragmentation during their respective fabrication processes, and have to reassemble once they have been embedded in

viscous hydrogels, a condition that may impair the onset of polarity across all organoids, as suggested by our results. These findings are also supported by the comparable trends observed in organoid viability post-fabrication (Figure 4), in which, much like for MDR-1 polarization, EBB showed the lowest values, followed by the milder casting process. In addition, Matrigel controls were also negative for MDR-1, and notably also for albumin, even if the marker was present at a gene expression level, indicating no synthesis of this protein and indicative of a well-known common mismatch in molecular biology between mRNA levels and actual protein expression.[57–59] This result, paired with the previous finding of enhanced metabolic activity over time, further underlines how Matrigel is an ideal substrate for organoid proliferation. On the other hand, for hepatocytic differentiation, other hydrogels[46,47,60] including gelMA as shown in this study, appear to provide a more suitable 3D environment. While the exact mechanism by which gelMA facilitates organoid differentiation remains to be elucidated, previous studies with other RGD-modified polyethylene-glycol hydrogels have identified stiffness values in the range between 1–2 kPa as beneficial for organoid growth and differentiation.[46] Conversely, the same hydrogels in softer or stiffer formulation lead to inferior organoid yield and expression of liver fibrosis markers, respectively.[46] Interestingly, gelMA-iodix-anol bioresins yielded gels with compressive moduli of 1.73 ± 0.09 kPa, nearly identical to the matrigel compressive modulus (1.72 ± 0.09 kPa), suggesting that mechanosensing may indeed be a contributing element to the enhanced organoid differentiation, and the biological cues provided by the gelatin-derived gelMA resin may be a key factor in creating a more permissive environment for differentiation compared to the proliferative enhancement observed in Matrigel culture systems. These soft gels are also likely a consequence of the higher sol-fraction after crosslinking, since unmodified gelMA prepared at the same prepolymer concentration with no optical tuning resulted in stiffer gels (5.04 ± 0.10 kPa) (Figure S11, Supporting Information). Notably, both gelMA resins were shown to remain biodegradable after the photocrosslinking process, as found upon exposure to a collagenase-laden media,[61] an essential characteristic of biocompatible materials used in the field of tissue engineering (Figure S12, Supporting Information).

Upon confirming that VBP samples in optically tuned gelMA bioresins provide a suitable environment for liver organoid differentiation, we investigated the potential of bioprinting to modulate the functionality of the organoid-laden constructs, when cultured in a dynamic perfusion setting. At first, we selected a series of 3D objects with convoluted pore distribution from a pool of mathematically defined triple periodic minimal surface structures. This class of geometries is well-known in the field of tissue engineering, as lattices belonging to this family have been investigated to produce mechanical metamaterials,[62] to maximize cell seeding in polymeric scaffolds,[63] and to promote in vivo bone ingrowth in biomaterials-based implants,[64] among other applications. Specifically, we selected three lattice structures with interconnected porosity: Schwarz D, Schwarz G, and Schwarz P.[65–68] At a comparable volume (between 383.17 and 394.25 mm³), these structures show a decrease in surface area to volume ratio (from 2.05 to 1.88 mm⁻¹), and decreasing average tortuosity of the porous

network (from 1.32 to 1.04) respectively. (Figure S13 and Table S5, Supporting Information). Thus, the choice of these structures provide the possibility to modulate key geometrical parameters, and, under perfusion, the flow profile within the porous construct, that are paramount for the interaction between the embedded cells and the solutes within the culture media, without significantly altering the cell content and cell density. Therefore, these architectures offer an ideal platform and proof-of-concept to study the effect of the geometry imposed by the printing process on the functionality of the embedded cells. Notably, such complex geometries are in general extremely difficult to reproduce at high resolution with extrusion technologies, especially when soft hydrogels are used as carrier materials. Hydrogel-based gyroidal structures can instead be easily printed with digital light projection bioprinting techniques, although generally requiring extended printing times that scale linearly with the height of the construct.[69]

However, printing similar convoluted structures in cell-friendly processing times and at the same time ensuring shape fidelity when using soft, cell-friendly hydrogels like the gelMA-iodixanol bioresin tested in this study remains a major challenge in the field of biofabrication. Via VBP, we could successfully generate all three Schwarz structures laden with organoids, and the construct could maintain their shape when retrieved from the printing environment and immersed in aqueous media. To facilitate handling and permit a seamless coupling of the constructs with a fluidic circuit for perfusion culture, we modified the design of the lattices. These were encased in a hydrogel-made fluidic chamber, equipped with an entry and an exit port, to which plastic microfluidic tubing could be coupled. The modified design could be reproducibly printed, with a printing time ranging from 14 to 15.5 s, depending on the geometry (**Figure 6**A, Videos S1–3, Supporting Information). When compared to the extensive printing times that would be needed to fabricate these same centimeter-scale structures under optimal printing conditions (between 24.7–34.0 min, even when using the easily printable and high-shape fidelity ink Pluronic F127, Figure S14, Supporting Information), the extremely rapid printing speed offered by VBP pose a promising advantage to overcome the detrimental effects on cell functionality that have been previously observed over extended printing times.[18] Given the high-speed printing achieved with VBP, these structures could also be printed for high-throughout analysis in a matter of minutes (Figure S15, Supporting Information). The system was first perfused with a constant flow of buffered solution supplemented with fluorescent microspheres to evaluate the flow profile within the structures. Tracking of the trajectory of the beads confirmed that these particles followed a nearly straight path in the Schwarz P lattice, as opposed to an increasingly wavy path in the other geometries (Figure 6B, Videos S4–6, Supporting Information). This was quantitatively proven by the significantly larger trajectory amplitudes exhibited by the Schwarz D structure (0.214 ± 0.098 mm) compared to the G and P architectures (0.157 ± 0.109 and 0.077 ± 0.105 mm respectively, Figure S16, Supporting Information). Given the constant flow rate (1.5 µL min^{-1}) imposed by the pump connected to the system and a smaller equivalent cross-sectional area along the flow pathway within more convoluted lattice in the Schwarz D, the average particle speed in this system was the highest

(0.416 ± 0.009 mm s^{-1}), whereas the lowest speed was found for the Schwarz P lattice (0.241 ± 0.009) (Figure 6C). Thus, the Schwarz D and P geometries, that showed the most marked differences in terms of flow profile, were printed embedding liver organoids, and conditioned in differentiation media, prior to being connected to the perfusion system for 24 h.

During this time, the culture media was collected to measure the secretion of albumin and of the liver-specific enzyme GLDH, which is a key player in protein catabolism, ammonia production, and in the generation of substrates for the synthesis of ATP (Figure 6D–F).[70] Albumin levels secreted over a 24 h period of continuous flow perfusion were highest in the Schwarz P structure (0.061 ± 0.051 mg mg$_{total-protein}^{-1}$) compared to Schwarz D (0.013 ± 0.008 mg mg$_{total-protein}^{-1}$) and static controls (0.002 ± 0.001 mg mg$_{total-protein}^{-1}$) (Figure 6D). The total albumin production (3.40 ± 1.75 and 17.00 ± 13.03 µg mL^{-1} for Schwarz D and P, respectively, Table S6, Supporting Information) exhibited by the complex printed structures was also superior to previously reported experimental results from liver-like constructs, where albumin values range from ≈ 0.004,[47] ≈ 0.3,[71,72] and ≈ 0.6 µg mL^{-1},[73] over longer medium collection periods of 7–10 days. Taking into account the total volume of medium collected in our perfusable system (≈ 28 mL), these highly complex VBP-printed biofactories outperform previous tissue engineering attempts in terms of albumin production. As for GLDH, printed and static constructs exhibited similar enzyme levels (Figure 6E). Most notably, the organoid-laden bioprinted lattices were able to actively remove ammonia from the media injected in the perfusion chamber (Figure 6G), a key function normally performed by the liver through the urea cycle. Ammonia detoxification was significantly higher under perfusion culture (33.5 ± 5.8 and 24.3 ± 1.4 nmol mg$_{total-protein}^{-1}$ for Schwarz D and P, respectively) when compared to static controls (12.7 ± 0.3 nmol mg$_{total\ protein}^{-1}$), suggesting that the applied flow promotes organoid function, possibly due to stimuli provided by the fluid shear stresses on the gelMA-embedded organoids. Previous studies using perfusion systems in combination with liver cell lines,[74] stem cells,[27] and differentiated primary cells[30] have shown enhanced liver-like functions in smaller-scale systems. In addition, fluid flow-induced shear stresses have demonstrated to enhance organoid maturation in different tissue engineering and organ-on-a-chip applications (i.e., kidney),[75] further supporting the hypothesis that shear stimuli also played a role in our system. Importantly, in Schwarz D samples, due to the higher flow velocity compared to the Schwarz P lattice, ammonia molecules have a shorter residency time within the construct (24.0 versus 41.5 s). Yet, ammonia elimination also occurred at a significantly faster rate, indicating that the ammonia detoxification capacity of the bioprinted organoids can be effectively boosted by the accurate selection of the architecture imposed to the organoid-laden hydrogel, in this case, using a highly convoluted, tortuous structure like the Schwarz D construct (Figure 6H). While it can be inferred that part of this modulation of the biological functionality in response to the engineered geometry can be due to an improved surface area available for exchange of solutes, it is also likely that the design-driven enhancement in diffusion could directly stimulate the encapsulated liver organoids. It should also be noted that, given the design of these
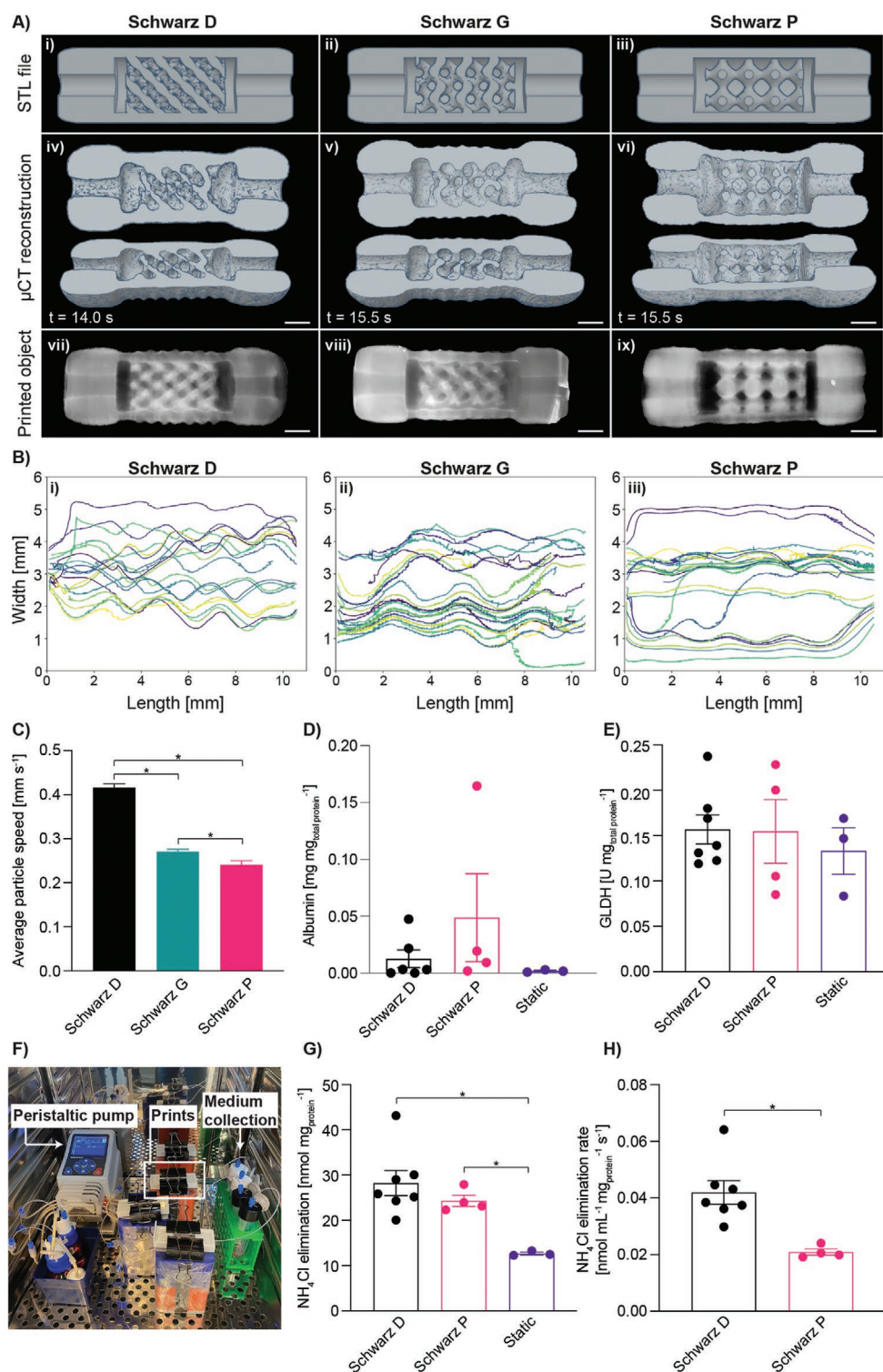
Figure 6. Modulating hepatic organoid function through volumetric bioprinting of mathematically derived lattices with differing flow properties. A) Complex, perfusable architectures are successfully printed within seconds with an adjusted lattice design that enables coupling to microfluidic tubing as shown in the STL models (i–iii) of the Schwarz D (i), Schwarz G (ii), and Schwarz P (iii) architectures. iv–vi) 3D reconstructions from µCT scans and vii–ix) macrophotographs showing the different complex and interconnected pore networks exhibited by the Schwarz D (iv,vii), G (v,viii), and P (vi,ix) structures (scale bars = 2 mm). B) These complex architectures are shown to modulate the flow trajectory of microspheres moving through the Schwarz D (i), G (ii), and P (iii) prints, as well as C) the average speed of the flowing particles ($n = 485$–1210). D) Albumin secretion and E) GLDH levels of organoids embedded in Schwarz D and P architectures, after 24 h of continuous perfusion ($n = 4$–8). F) Sterile perfusion setup, which enabled perfusion of differentiation medium supplemented with 1.5×10^{-3} M NH_4Cl through complex architectures and resulted in G) differing total NH_4Cl elimination compared to statically cultured cylindrical control samples and H) architecture-dependent NH_4Cl elimination rates ($n = 4$–8). * = significant difference ($p < 0.05$).

**ADVANCED
SCIENCE NEWS**

www.advancedsciencenews.com

**ADVANCED
MATERIALS**

www.advmat.de

constructs, organoids were also present in the casing with connectors placed around the lattices, and these additions to the Schwarz structures were identical for all three architectures. Nevertheless, the variation in geometry imparted in the central part of the object was sufficient to observe a difference in terms of cell behavior during culture. In the context of our in vitro system, these mathematically defined lattices were shown to offer unique potential to control the fluid flow within the pores and to modulate the communication between the bioprinted organoids and solutes found in the media, leading to a modulatory effect on ammonia detoxification. Moreover, it is important to remark that, although in this specific study focused on bioprinting for in vitro 3D culture applications, and thus in vivo regenerative medicine applications go beyond the scope of this work, such user designable, bioprinted structures that can maximize the ability of the cells to interact with the surrounding nutrients and signals could have valuable applications also for producing transplantable grafts. Overall, these results underline the importance of architectural cues in the design of advanced tissue-engineered and biofabricated constructs.

3. Conclusions

The first phase of the study takes fundamental steps to unravel the effects of different cellular components (single cells and organoids) on the volumetric printing process, namely due to the cell-mediated light scattering and its effect on printing resolution. Using this knowledge, an optically tuned, gelatin-based bioresin was successfully developed and was able to reduce scattering through refractive index matching of specific intracellular components. This strategy is versatile, and could be potentially applied to resins used for volumetric additive manufacturing which use other photocrosslinking chemistries besides methacryloyl-based, such as thiol-ene step growth.[76] This development allowed high resolution volumetric bioprinting with increasing cell densities, and provides important knowledge on the ideal design requirements for the development of next-generation bioresins for VBP. In combination with more advanced tomographic algorithms, multi-material and multi-cellular printing approaches can be more easily established in order to increase the overall complexity of volumetrically printed architectures. Using the liver as a model tissue platform, this study demonstrated the ability to harness the advantages of both VBP and organoid technology in a single approach that resulted in the fabrication of multi-scale biofactories capable of guiding tissue-specific functions. Liver-derived organoids were successfully printed at high densities and demonstrated maintained viability and hepatic function compared to extrusion printed and cast controls. The layerless fabrication approach employed by VBP resulted in increased organoid viability post-printing, and enabled the preservation of organoid morphology and polarity compared to controls. The soft, organoid-laden bioresin was successfully sculpted into highly convoluted, mathematically derived structures with distinct structural properties. Successful printing of these cell-laden structures in under 20 s and establishment of a sterile perfusion chamber allowed the printed organoids to act as biofactories capable of modulating liver-specific ammonia detoxi-

fication depending on the printed architecture. These findings demonstrate the close relationship between the shape of the constructs and their resulting biological functionality, further underlining the potential of biofabrication for advancing tissue engineering. This study, therefore, opens up new possibilities for the future development of self-sustaining biofactories that are able to carry out a wide variety to tissue-specific functions. Overall, the combination of the ultrafast VBP process with organoid technology holds great potential for the development of advanced regenerative medicine approaches and in vitro model development for fundamental biology research, personalized drug screening, and disease modeling.

4. Experimental Section

Materials: gelMA (93.5% DoF) was synthesized as previously reported,[77] and used as a 5% w/v solution in phosphate-buffered saline (PBS). Lithium phenyl(2,4,6-trimethylbenzoyl)phosphinate (LAP, Tokyo Chemical Industry, Japan) was added at 0.1% (w/v) as a photoinitiator to induce a photocrosslinking reaction. To perform optical tuning of the cell-laden bioresin, the gelMA and LAP solution was supplemented with different concentrations (0–40% w/v) of iodixanol (OptiPrep; StemCell Technologies, Canada).

Volumetric Bioprinting Procedure: Volumetric bioprinting of different structures was achieved using a Tomolite printer (Readily3D, Switzerland). For bioprinting, single cells and hepatic organoids were embedded in different gelMA bioresins at densities of 1–1.5 × 10^7 cells per mL and placed in Ø10 mm cylindrical borosilicate glass vials. The bioresin-filled vials were placed at 4 °C to elicit thermal gelation and prevent cell sedimentation throughout the printing process. Briefly, the printing process was induced by a laser beam at 405 nm directed onto a DMD that was modulated into tomographic projections. These projections were then imaged into the printing vials. The projections were calculated using a commercial software (Apparite, Readily3D, Switzerland) taking into account the material properties of the resin and the printing vials. The average light intensity before the printing container was 9.98 mW cm^−2 during printing. Further details concerning the tomographic printing process can be found in literature.[16,17] Post-printing, the printer vials were heated to 37 °C to melt the unpolymerized bioresin, and samples were washed with prewarmed PBS. For the printing optimization experiments, prints at different light doses were performed, by modulating the exposure time. Successful crosslinking was appreciated for doses at which every intended feature object could be resolved and the print did not redissolve when heating the bioresin. Finally, the as-printed parts underwent 5 min of additional crosslinking in 0.1% w/v LAP in PBS solution in a CL-1000 Ultraviolet Crosslinker (λ = 365 nm; UVP, USA).

Hepatic Organoid Establishment, Expansion, and Differentiation: Healthy liver biopsies were obtained during liver transplantation at the Erasmus Medical Center Rotterdam in accordance with the ethical standard of the institutional committee to use the tissue for research purposes (ethical approval number MEC 2014-060). The procedure was in accordance with the Helsinki Declaration of 1975 and informed consent in writing was obtained from each patient. Disposable 125-mL spinner flasks (Corning, USA) were inoculated with 5 × 10^6 of the collected single cells in 20 mL expansion medium (EM), including 10% v/v Matrigel (Corning, New York, NY, USA) to increase organoid yield as previously described.[44] Rotation speed was set to 85 rpm. Every 2–3 days, new medium was added to the spinner flasks. After a 14-day expansion period, organoids were collected for printing and passaged into a new spinner flask. To assess the size of the organoids, aliquots from the spinner flasks were taken at the end of the culture time and imaged with an optical microscope, measuring the diameter of at least 150 organoids per spinner flask. In order to match the printed cell densities to the single cell conditions, aliquots of the organoid suspension were mechanically

fragmented and trypsinized into single cells, and were subsequently counted using an automatic cell counter. Post-printing, organoid-laden structures were cultured in hepatic differentiation media (DM) for 10 days. For single cell studies, HepG2 cell line was used, (ATCC nr. HB-8065) and cultured in T175 culture flasks in HEPG2 EM, which was replenished twice a week. All cultures were kept in a humidified atmosphere of 95% air and 5% CO_2 at 37 °C. Details of the cell isolation protocol from liver biopsies and of the culture media components are reported in the Supporting Information.

Stereomicroscopy and Computed Tomography for Print Evaluation: Macroscopic images of cell- and organoid-laden structures were acquired using an Olympus SZ61 stereomicroscope coupled with an Olympus DP70 digital camera (Olympus Soft Imaging Solutions GmbH, The Netherlands). Zoomed-in images were cropped and pasted over a black background to eliminate background reflections. μCT scans were performed with a Quantum FX μCT (voxel size = 15 μm³, 90 kV tube voltage, 200 μA current, and 26 s of scan time, Perkin Elmer, USA). 3D reconstructions were generated with the 3D viewer plugin in Image J ($n = 3$–6).

Refractive Index and Measurements of Scattering Phase Function of Cell Suspensions: The refractive index of bioresins with different iodixanol concentrations ($n = 3$) was measured with an Abbe refractometer (2WAJ, Optika, Italy). The scattering properties of the hydrogels were measured with a custom-made apparatus, as depicted in Figure 3D. The principle of the setup was similar to that introduced by Hunt and Huffman.[78] The apparatus setup and anisotropy coefficient calculations are detailed in the Supporting Information.

Metabolic Activity and Viability of Bioprinted and Cast Organoids: Cylindrical organoid-laden constructs (5×10^6 cells mL^{-1}; 5 mm diameter × 2 mm height) were produced through: i) volumetric bioprinting (170 mJ cm^{-2}, 17.0 s printing time) with and without iodixanol (0–40% w/v), ii) EBB with a pneumatic-driven system (25 G stainless-steel nozzle, temperature = 21 °C, pressure = 0.03 MPa, 3DDiscovery, REGENHU, Switzerland), iii) casting of the gelMA bioresin with and without iodixanol (10% w/v) and crosslinking for 15 min in a CL-1000 Ultraviolet Crosslinker (λ = 365 nm; UVP, USA) and iv) casting in Matrigel droplets, thermally crosslinked at 37 °C for 20 min. Importantly, EBB-printed organoids had to be mechanically fragmented using a P200 pipette tip in order to prevent nozzle clogging prior to the fabrication step. Samples were cultured in organoid differentiation medium for 10 days, which was refreshed every two days. Metabolic activity ($n = 5$) was measured with a resazurin assay (resazurin sodium salt, Alfa Aesar, Germany) and normalized by double-stranded DNA content per sample quantified using a Picogreen Quant-iT assay (Thermo Fischer Scientific, The Netherlands) after 1, 3, 7 and 10 days. Cell viability was evaluated using a live/dead assay (Calcein, ethidium homodimer, Thermo Fischer Scientific, The Netherlands) after 1, 3, and 10 days ($n = 3$), imaged by a Thunder imaging system (Leica Microsystems, Germany). For each measurement in the printing/casting comparisons, 3 donors were evaluated ($N = 3$).

Hepatic Functionality Assessment of Bioprinted/Cast Constructs: CYP3A4 activity in organoids at day 10 of differentiation was quantified using the P450-Glo CYP3A4 Assay (Promega, USA) according to the manufacturer's instructions. CYP3A4 levels were normalized to DNA amount in the samples determined with a picogreen assay ($n = 3$). Gene expression of liver-specific markers (CYP3A4 and albumin) was quantified through RT-qPCR (Bio-Rad, The Netherlands) at day 10 of differentiation ($n = 3$). Liver-specific and polarization marker expression upon hepatic differentiation (HNF4α, ZO-1, MDR1, CK-19, and E-cadherin) were visualized through immunofluorescent stainings and imaged using a Thunder imaging system (Leica Microsystems, Germany) ($n = 3$). Details of the qPCR protocol primers and of the immunohistochemical procedures are reported in the Supporting Information. Liver transaminase and GLDH present in organoid-laden constructs and secreted albumin in the culture medium were measured with the clinical chemistry analyzer Beckman AU680 (Beckman Coulter, USA) using standard protocols ($n = 3$). Values were normalized to total protein content quantified through a micro-BCA protein assay kit (ThermoFischer Scientific, The Netherlands).

Fluorescent Beads Tracking through Complex Printed Structures: Printed Schwarz D, G, and P strcutures were placed in a custom-made PDMS mold and connected to a syringe pump using FA microfluidic tubing (IDEX Health&Science, OD 1.6 mm, ID 0.75 mm). Green fluorescent polyethylene microspheres (125–150 μm diameter; Cospheric, USA) were perfused through the printed structures at a flow rate of 20 μL min^{-1} ($n = 3$). Videos of microsphere flow through the printed constructs were recorded using a custom-made imaging system (Supporting Information). The particle trajectories were calculated from the acquired videos with the Crocker and Grier algorithm,[79] using trackpy v0.5.0 (https://zenodo.org/record/4682814). The particles identified in each video frame were linked into trajectories using a proximity criterion. Mean particle speeds were calculated as averages between each trajectory start and end point, where the contribution of each trajectory to the overall mean speed was weighed by the trajectory length. The amplitude was calculated on a subset of the oscillations within the trajectories shown in Figure 6B-i–iii ($n = 50$–80). Local minima and maxima values were identified in the trajectory y positions. Amplitude was calculated as half of the distance in the direction orthogonal to the main direction of the flow from a maximum to the subsequent minimum. All code used for video analysis is available at: https://github.com/VictorOnink/Particle-Trajectory-Analysis.

Ammonia Elimination Assay in a Sterile Perfusion Setup: Organoid-laden, volumetrically bioprinted Schwarz D and P structures (5×10^6 cells mL^{-1}, 200 mJ cm^{-2}, 20.0 s printing time; $n = 8$ and 4 respectively) were cultured with differentiation medium for 10 days under static conditions. After 10 days the structures were transferred to a sterile flow perfusion chamber (Supporting Information) and perfused with DM supplemented with 1.5×10^{-3} M ammonium chloride (NH$_4$Cl) for 24 h under continuous flow of 20 μL min^{-1}. The fluidic chambers were cultured in sterile conditions at 37 °C, and medium was collected for 24 h. Ammonium chloride concentrations in the collected medium were determined using a Urea/Ammonia Assay Kit (Megazyme, Ireland). Medium samples were decolored using activated carbon (Merck, Germany). Static controls consisted of volumetrically printed non-porous cylinders (diameter 6 mm × 17 mm height) cultured under static conditions ($n = 3$). Media supplemented with 1.5×10^{-3} M NH$_4$Cl that was incubated for 24 h without cells was used to determine the initial concentration ($n = 3$). Total ammonium chloride elimination and elimination rate were normalized to the total protein content.

Statistics: Results were reported as mean ± standard error of the mean (S.E.M.). Statistical analysis was performed using GraphPad Prism 9.0 (GraphPad Software, USA). Comparisons between experimental groups were assessed via one or two-way ANOVAs, followed by post hoc Bonferroni correction to test differences between groups. When normality could not be assumed, non-parametric tests were performed. Differences were found to be significant when $p < 0.05$.

Supporting Information

Supporting Information is available from the Wiley Online Library or from the author.

Acknowledgements

**ADVANCED
SCIENCE NEWS**

www.advancedsciencenews.com

**ADVANCED
MATERIALS**

www.advmat.de

Conflict of Interest

Dr. P. Delrot and Dr. D. Loterie are shareholders and employees of Readily3D SA. Prof. C. Moser is a shareholder of Readily3D SA. All the other co-authors declare no conflicts of interest.

Data Availability Statement

The data that support the findings of this study are available from the corresponding author upon reasonable request.

Keywords

biofabrication, bioresins, hydrogels, light-based 3D printing, volumetric additive manufacturing

[1] V. Mironov, T. Trusk, V. Kasyanov, S. Little, R. Swaja, R. Markwald, *Biofabrication* **2009**, *1*, 022001.

[2] R. Levato, T. Jungst, R. G. Scheuring, T. Blunk, J. Groll, J. Malda, *Adv. Mater.* **2020**, *32*, 1906423.

[3] J. Groll, T. Boland, T. Blunk, J. A. Burdick, D.-W. W. Cho, P. D. Dalton, B. Derby, G. Forgacs, Q. Li, V. A. Mironov, L. Moroni, M. Nakamura, W. Shu, S. Takeuchi, G. Vozzi, T. B. F. F. Woodfield, T. Xu, J. J. Yoo, J. Malda, *Biofabrication* **2016**, *8*, 013001.

[4] M. M. Laronda, A. L. Rutz, S. Xiao, K. A. Whelan, F. E. Duncan, E. W. Roth, T. K. Woodruff, R. N. Shah, *Nat. Commun.* **2017**, *8*, 15261.

[5] E. A. Bulanova, E. V. Koudan, J. Degosserie, C. Heymans, F. D. A. S. Pereira, V. A. Parfenov, Y. Sun, Q. Wang, S. A. Akhmedova, I. K. Sviridova, N. S. Sergeeva, G. A. Frank, Y. D. Khesuani, C. E. Pierreux, V. A. Mironov, *Biofabrication* **2017**, *9*, 034105.

[6] J. H. Kim, I. Kim, Y. J. Seol, I. K. Ko, J. J. Yoo, A. Atala, S. J. Lee, *Nat. Commun.* **2020**, *11*, 1025.

[7] I. Martin, J. Malda, N. C. Rivron, *Curr. Opin. Organ Transplant.* **2019**, *24*, 562.

[8] P. L. Lewis, R. M. Green, R. N. Shah, *Acta Biomater.* **2018**, *69*, 63.

[9] H. Clevers, *Cell* **2016**, *165*, 1586.

[10] J. Kim, B. K. Koo, J. A. Knoblich, *Nat. Rev. Mol. Cell Biol.* **2020**, *21*, 571.

[11] P. N. Bernal, P. Delrot, D. Loterie, Y. Li, J. Malda, C. Moser, R. Levato, *Adv. Mater.* **2019**, *31*, 1904209.

[12] A. Marsee, F. J. M. Roos, M. M. A. Verstegen, F. Roos, M. Verstegen, H. Clevers, L. Vallier, T. Takebe, M. Huch, W. C. Peng, S. Forbes, F. Lemaigre, E. de Koning, H. Gehart, L. van der Laan, B. Spee, S. Boj, P. Baptista, K. Schneeberger, C. Soroka, M. Heim, S. Nuciforo, K. Zaret, Y. Saito, M. Lutolf, V. Cardinale, B. Simons, S. van IJzendoorn, A. Kamiya, H. Chikada, et al., *Cell Stem Cell* **2021**, *28*, 816.

[13] M. Huch, H. Gehart, R. Van Boxtel, K. Hamer, F. Blokzijl, M. M. A. Verstegen, E. Ellis, M. Van Wenum, S. A. Fuchs, J. De Ligt, M. Van De Wetering, N. Sasaki, S. J. Boers, H. Kemperman, J. De Jonge, J. N. M. Ijzermans, E. E. S. Nieuwenhuis, R. Hoekstra, S. Strom, R. R. G. Vries, L. J. W. Van Der Laan, E. Cuppen, H. Clevers, *Cell* **2015**, *160*, 299.

[14] S. P. Harrison, S. F. Baumgarten, R. Verma, O. Lunov, A. Dejneka, G. J. Sullivan, *Front. Med.* **2021**, *8*, 574047.

[15] B. E. Kelly, I. Bhattacharya, H. Heidari, M. Shusteff, C. M. Spadaccini, H. K. Taylor, *Science* **2019**, *363*, 1075.

[16] D. Loterie, P. Delrot, C. Moser, *Nat. Commun.* **2020**, *11*, 852.

[17] P. N. Bernal, P. Delrot, D. Loterie, Y. Li, J. Malda, C. Moser, R. Levato, *Adv. Mater.* **2019**, *31*, 1904209.

[18] M. de Ruijter, A. Ribeiro, I. Dokter, M. Castilho, J. Malda, *Adv. Healthcare Mater.* **2019**, *8*, 1800418.

[19] A. Schwab, R. Levato, M. D'Este, S. Piluso, D. Eglin, J. Malda, *Chem. Rev.* **2020**, *120*, 11028.

[20] A. Ribeiro, M. M. Blokzijl, R. Levato, C. W. Visser, M. Castilho, W. E. Hennink, T. Vermonden, J. Malda, *Biofabrication* **2017**, *10*, 014102.

[21] N. Paxton, W. Smolan, T. Böck, F. Melchels, J. Groll, T. Jungst, *Biofabrication* **2017**, *9*, 044107.

[22] C. Echalier, R. Levato, M. A. A. Mateos-Timoneda, O. Castaño, S. Déjean, X. Garric, C. Pinese, D. Noël, E. Engel, J. Martinez, A. Mehdi, G. Subra, *RSC Adv.* **2017**, *7*, 12231.

[23] P. Arjmand, O. Katz, S. Gigan, M. Guillon, *Opt. Express* **2021**, *29*, 6563.

[24] D. Loterie, P. Delrot, C. Moser, *ResearchGate* **2018**, https://org/0.13140/RG.2.2.20027.46889.

[25] R. Rizzo, D. Ruetsche, H. Liu, M. Zenobi-Wong, *Adv. Mater.* **2021**, *33*, 2102900.

[26] S. P. Rebelo, R. Costa, M. Estrada, V. Shevchenko, C. Brito, P. M. Alves, *Arch. Toxicol.* **2015**, *89*, 1347.

[27] V. Starokozhko, M. Hemmingsen, L. Larsen, S. Mohanty, M. Merema, R. C. Pimentel, A. Wolff, J. Emnéus, A. Aspegren, G. Groothuis, M. Dufva, *J. Tissue Eng. Regener. Med.* **2018**, *12*, 1273.

[28] J. Christoffersson, C. Aronsson, M. Jury, R. Selegård, D. Aili, C. F. Mandenius, *Biofabrication* **2019**, *11*, 015013.

[29] M. Kehtari, B. Zeynali, M. Soleimani, M. Kabiri, E. Seyedjafari, *Artif. Cells, Nanomed., Biotechnol.* **2018**, *46*, 161.

[30] M. B. Esch, J. M. Prot, Y. I. Wang, P. Miller, J. R. Llamas-Vidales, B. A. Naughton, D. R. Applegate, M. L. Shuler, *Lab Chip* **2015**, *15*, 2269.

[31] L. E. Bertassoni, J. C. Cardoso, V. Manoharan, A. L. Cristino, N. S. Bhise, W. A. Araujo, P. Zorlutuna, N. E. Vrana, A. M. Ghaemmaghami, M. R. Dokmeci, A. Khademhosseini, *Biofabrication* **2014**, *6*, 024105.

[32] A. Mazzocchi, M. Devarasetty, R. Huntwork, S. Soker, A. Skardal, *Biofabrication* **2019**, *11*, 015003.

[33] R. Taymour, D. Kilian, T. Ahlfeld, M. Gelinsky, A. Lode, *Sci. Rep.* **2021**, *11*, 5130.

[34] H. Lee, W. Han, H. Kim, D. H. Ha, J. Jang, B. S. Kim, D. W. Cho, *Biomacromolecules* **2017**, *18*, 1229.

[35] S. Hong, J. M. Song, *Biomater. Sci.* **2021**, *9*, 5939.

[36] J. Madrid-Wolff, A. Boniface, D. Loterie, P. Delrot, C. Moser arXiv: 2105.14952, **2021**.

[37] T. Boothe, L. Hilbert, M. Heide, L. Berninger, W. B. Huttner, V. Zaburdaev, N. L. Vastenhouw, E. W. Myers, D. N. Drechsel, J. C. Rink, *eLife* **2017**, *6*, e27240.

[38] B. Pouran, V. Arbabi, R. L. Bleys, P. René van Weeren, A. A. Zadpoor, H. Weinans, *J. Biomech.* **2017**, *52*, 148.

2110054 (15 of 16)

**ADVANCED
SCIENCE NEWS**

www.advancedsciencenews.com

**ADVANCED
MATERIALS**

www.advmat.de

[39] M. I. Zonneveld, M. J. C. van Herwijnen, M. M. Fernandez-Gutierrez, A. Giovanazzi, A. M. de Groot, M. Kleinjan, T. M. M. van Capel, A. J. A. M. Sijts, L. S. Taams, J. Garssen, E. C. de Jong, M. Kleerebezem, E. N. M. Nolte-'t Hoen, F. A. Redegeld, M. H. M. Wauben, *J. Extracell. Vesicles* **2021**, *10*, e12071.

[40] P. Y. Liu, L. K. Chin, W. Ser, H. F. Chen, C. M. Hsieh, C. H. Lee, K. B. Sung, T. C. Ayi, P. H. Yap, B. Liedberg, K. Wang, T. Bourouina, Y. Leprince-Wang, *Lab Chip* **2016**, *16*, 634.

[41] W. M. Lee, *N. Engl. J. Med.* **2003**, *349*, 474.

[42] H. Olson, G. Betton, D. Robinson, K. Thomas, A. Monro, G. Kolaja, P. Lilly, J. Sanders, G. Sipes, W. Bracken, M. Dorato, K. Van Deun, P. Smith, B. Berger, A. Heller, *Regul. Toxicol. Pharmacol.* **2000**, *32*, 56.

[43] S. P. den Braver-Sewradj, M. W. den Braver, M. van Dijk, Y. Zhang, S. J. Dekker, L. Wijaya, N. P. E. Vermeulen, L. Richert, J. N. M. Commandeur, J. C. Vos, *Curr. Drug Metab.* **2018**, *19*, 370.

[44] K. Schneeberger, N. Sánchez-Romero, S. Ye, F. G. van Steenbeek, L. A. Oosterhoff, I. Pla Palacin, C. Chen, M. E. van Wolferen, G. van Tienderen, R. Lieshout, H. Colemonts-Vroninks, I. Schene, R. Hoekstra, M. M. A. Verstegen, L. J. W. van der Laan, L. C. Penning, S. A. Fuchs, H. Clevers, J. De Kock, P. M. Baptista, B. Spee, *Hepatology* **2020**, *72*, 257.

[45] K. Schneeberger, B. Spee, P. Costa, N. Sachs, H. Clevers, J. Malda, *Biofabrication* **2017**, *9*, 013001.

[46] G. Sorrentino, S. Rezakhani, E. Yildiz, S. Nuciforo, M. H. Heim, M. P. Lutolf, K. Schoonjans, *Nat. Commun.* **2020**, *11*, 3416.

[47] M. Krüger, L. A. Oosterhoff, M. E. van Wolferen, S. A. Schiele, A. Walther, N. Geijsen, L. De Laporte, L. J. W. van der Laan, L. M. Kock, B. Spee, *Adv. Healthcare Mater.* **2020**, *9*, 1901658.

[48] A. Blaeser, D. F. Duarte Campos, U. Puster, W. Richtering, M. M. Stevens, H. Fischer, *Adv. Healthcare Mater.* **2016**, *5*, 326.

[49] R. Levato, J. Visser, J. A. Planell, E. Engel, J. Malda, M. A. Mateos-Timoneda, *Biofabrication* **2014**, *6*, 035020.

[50] J. A. Brassard, M. Nikolaev, T. Hübscher, M. Hofer, M. P. Lutolf, *Nat. Mater.* **2021**, *20*, 22.

[51] Y. Liu, C. Dabrowska, A. Mavousian, B. Strauss, F. Meng, C. Mazzaglia, K. Ouaras, C. Macintosh, E. Terentjev, J. H. Lee, Y. Y. S. Huang, *Adv. Sci.* **2021**, *8*, 2003332.

[52] A. C. Daly, M. D. Davidson, J. A. Burdick, *Nat. Commun.* **2021**, *12*, 753.

[53] S. A. Ferreira, M. S. Motwani, P. A. Faull, A. J. Seymour, T. T. L. Yu, M. Enayati, D. K. Taheem, C. Salzlechner, T. Haghighi, E. M. Kania, O. P. Oommen, T. Ahmed, S. Loaiza, K. Parzych, F. Dazzi, O. P. Varghese, F. Festy, A. E. Grigoriadis, H. W. Auner, A. P. Snijders, L. Bozec, E. Gentleman, *Nat. Commun.* **2018**, *9*, 4049.

[54] R. Ouchi, S. Togo, M. Kimura, T. Shinozawa, M. Koido, H. Koike, W. Thompson, R. A. Karns, C. N. Mayhew, P. S. McGrath, H. A. McCauley, R. R. Zhang, K. Lewis, S. Hakozaki, A. Ferguson, N. Saiki, Y. Yoneyama, I. Takeuchi, Y. Mabuchi, C. Akazawa, H. Y. Yoshikawa, J. M. Wells, T. Takebe, *Cell Metab.* **2019**, *30*, 374.

[55] N. Sachs, J. de Ligt, O. Kopper, E. Gogola, G. Bounova, F. Weeber, A. V. Balgobind, K. Wind, A. Gracanin, H. Begthel, J. Korving, R. van Boxtel, A. A. Duarte, D. Lelieveld, A. van Hoeck, R. F. Ernst, F. Blokzijl, I. J. Nijman, M. Hoogstraat, M. van de Ven, D. A. Egan, V. Zinzalla, J. Moll, S. F. Boj, E. E. Voest, L. Wessels, P. J. van Diest, S. Rottenberg, R. G. J. Vries, E. Cuppen, et al., *Cell* **2018**, *172*, 373.

[56] R. J. Schulze, M. B. Schott, C. A. Casey, P. L. Tuma, M. A. McNiven, *J. Cell Biol.* **2019**, *218*, 2096.

[57] C. Vogel, E. M. Marcotte, *Nat. Rev. Genet.* **2012**, *13*, 227.

[58] T. Maier, M. Güell, L. Serrano, *FEBS Lett.* **2009**, *583*, 3966.

[59] R. De Sousa Abreu, L. O. Penalva, E. M. Marcotte, C. Vogel, *Mol. BioSyst.* **2009**, *5*, 1512.

[60] S. Ye, J. W. B. Boeter, M. Mihajlovic, F. G. van Steenbeek, M. E. van Wolferen, L. A. Oosterhoff, A. Marsee, M. Caiazzo, L. J. W. van der Laan, L. C. Penning, T. Vermonden, B. Spee, K. Schneeberger, *Adv. Funct. Mater.* **2020**, *30*, 2000893.

[61] R. Levato, K. S. Lim, W. Li, A. U. Asua, L. B. Peña, M. Wang, M. Falandt, P. N. Bernal, D. Gawlitta, Y. S. Zhang, T. B. F. Woodfield, J. Malda, *Mater. Today Bio* **2021**, *12*, 100162.

[62] S. J. P. Callens, C. H. Arns, A. Kuliesh, A. A. Zadpoor, *Adv. Funct. Mater.* **2021**, *31*, 2101373.

[63] F. P. W. Melchels, B. Tonnarelli, A. L. Olivares, I. Martin, D. Lacroix, J. Feijen, D. J. Wendt, D. W. Grijpma, *Biomaterials* **2011**, *32*, 2878.

[64] A. Paré, B. Charbonnier, P. Tournier, C. Vignes, J. Veziers, J. Lesoeur, B. Laure, H. Bertin, G. De Pinieux, G. Cherrier, J. Guicheux, O. Gauthier, P. Corre, D. Marchat, P. Weiss, *ACS Biomater. Sci. Eng.* **2020**, *6*, 553.

[65] S. C. Kapfer, S. T. Hyde, K. Mecke, C. H. Arns, G. E. Schröder-Turk, *Biomaterials* **2011**, *32*, 6875.

[66] T. Femmer, A. J. C. Kuehne, M. Wessling, *Chem. Eng. J.* **2015**, *273*, 438.

[67] Y. Jung, S. Torquato, *Phys. Rev. E* **2005**, *72*, 056319.

[68] N. Thomas, N. Sreedhar, O. Al-Ketan, R. Rowshan, R. K. Abu Al-Rub, H. Arafat, *Desalination* **2018**, *443*, 256.

[69] K. S. Lim, R. Levato, P. F. Costa, M. D. Castilho, C. R. Alcala-Orozco, K. M. A. Van Dorenmalen, F. P. W. Melchels, D. Gawlitta, G. J. Hooper, J. Malda, T. B. F. Woodfield, *Biofabrication* **2018**, *10*, 034101.

[70] A. Plaitakis, E. Kalef-Ezra, D. Kotzamani, I. Zaganas, C. Spanaki, *Biology* **2017**, *6*, 11.

[71] G. Hong, J. Kim, H. Oh, S. Yun, C. M. Kim, Y. M. Jeong, W. S. Yun, J. H. Shim, I. Jang, C. Y. Kim, S. Jin, *Adv. Mater.* **2021**, *33*, 2102624.

[72] D. Kang, G. Hong, S. An, I. Jang, W.-S. Yun, J.-H. Shim, S. Jin, *Small* **2020**, *16*, 1905505.

[73] M. Cuvellier, F. Ezan, H. Oliveira, S. Rose, J. C. Fricain, S. Langouët, V. Legagneux, G. Baffet, *Biomaterials* **2021**, *269*, 120611.

[74] Y. S. Kim, A. Asif, A. R. Chethikkattuveli Salih, J. W. Lee, K. N. Hyun, K. H. Choi, *Biomedicines* **2021**, *9*, 1369.

[75] K. A. Homan, N. Gupta, K. T. Kroll, D. B. Kolesky, M. Skylar-Scott, T. Miyoshi, D. Mau, M. T. Valerius, T. Ferrante, J. V. Bonventre, J. A. Lewis, R. Morizane, *Nat. Methods* **2019**, *16*, 255.

[76] C. C. Cook, E. J. Fong, J. J. Schwartz, D. H. Porcincula, A. C. Kaczmarek, J. S. Oakdale, B. D. Moran, K. M. Champley, C. M. Rackson, A. Muralidharan, R. R. McLeod, M. Shusteff, *Adv. Mater.* **2020**, *32*, 2003376.

[77] K. S. Lim, F. Abinzano, P. N. Bernal, A. Albillos Sanchez, P. Atienza-Roca, I. A. Otto, Q. C. Peiffer, M. Matsusaki, T. B. F. Woodfield, J. Malda, R. Levato, *Adv. Healthcare Mater.* **2020**, *9*, 1901792.

[78] A. J. Hunt, D. R. Huffman, *Rev. Sci. Instrum.* **1973**, *44*, 1753.

[79] J. C. Crocker, D. G. Grier, *J. Colloid Interface Sci.* **1996**, *179*, 298.